Journal of Inorganic Biochemistry 260 (2024) 112703

Contents lists available at ScienceDirect

Journal of Inorganic Biochemistry

journal homepage: www.elsevier.com/locate/jinorgbio

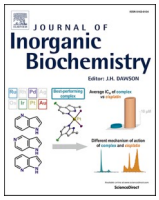

Enhanced DNA damage and anti-proliferative activity of a novel ruthenium complex with a chlorambucil-decorated ligand

Alberto Gobbo [a,1], Feihong Chen [b,1], Stefano Zacchini [c], Shaohua Gou [b,*], Fabio Marchetti [a,*]

[a] University of Pisa, Department of Chemistry, and Industrial Chemistry, Via G. Moruzzi 13, I-56124 Pisa, Italy
[b] Jiangsu Province Hi-Tech Key Laboratory for Biomedical Research, and School of Chemistry and Chemical Engineering, Southeast University, Nanjing 211189, PR China
[c] University of Bologna, Department of Industrial Chemistry "Toso Montanari", Via P. Gobetti 85, I-40129 Bologna, Italy

ARTICLE INFO

Keywords:
Ruthenium(II) complexes
Chlorambucil
Tris-Pyrazolylmethane
Anticancer activity
DNA damage

ABSTRACT

Triphenylphosphine substitution reactions of [RuCl(PPh$_3$)$_2$(tpm)]Cl, **1**, featuring tris(pyrazolyl)methane (tpm) as ligand, with the chlorambucil-decorated pyridine ligand **Py^{CA}**, 3-aminopyridine (**Py^{NH2}**) and 4-pyridinemethanol (**Py^{OH}**) afforded the corresponding pyridine complexes **2–4** in high yields. **Py^{CA}** was preliminarily obtained *via* esterification of 4-pyridinemethanol with chlorambucil. The new compounds **Py^{CA}** and **2–3** were characterized by IR and multinuclear NMR spectroscopy. Additionally, the structure of **3** was ascertained by single crystal X-ray diffraction. The *in vitro* anti-proliferative activity of **2–4** and **Py^{CA}** was determined against a panel of cancer cell lines, outlining **2** as the most performing compound. Targeted studies were subsequently undertaken using **2** to elucidate mechanistic aspects, including the assessment of ruthenium cellular uptake, cell cycle arrest, production of reactive oxygen species (ROS), western blotting and DNA damage (comet test). Overall, data highlight that the anticancer activity provided by **2** primarily affects the mitochondria pathway with a potential additional contribution from DNA damage.

1. Introduction

Intensive research efforts are underway to discover new metal-based anticancer drugs [1–3] that can overcome limitations [4–6] associated with currently employed platinum chemotherapics in clinical treatments [7–9]. In this setting, ruthenium complexes have garnered significant interest over the last few decades [10–14], due to their diverse structural motifs and limited toxicity in the human body [15,16].

Some ruthenium(III) complexes entered clinical trials [17–19], functioning as pro-drugs that undergo Ru^{III} to Ru^{II} reduction under the hypoxic conditions of tumor environments, thereby activating the species [20]. Inspired by this concept, various organometallic Ru^{II} complexes have shown promising potential as prospective antitumor drugs [21]. In particular, complexes belonging to the RAPTA family have emerged, configuring them for use in combination with other chemotherapics [22,23]. While many Ru^{II} arene complexes have been considered, their possible, rapid disassembly in physiological media [24,25] may limit effectiveness and introduce uncertain speciation that could lead to undesired collateral effects [26].

As an alternative, more robust species can be constructed based on the ruthenium-cyclopentadienyl framework, where the bonding of the Cp ligand (Cp = η^5-C$_5$H$_5$) to the metal benefits from an additional electrostatic contribution compared to the Ru-arene linkage [27,28]. Our recent investigations have unveiled the anticancer potential of ruthenium(II) tris(pyrazolyl)methane (tpm) complexes, which had remained largely unexplored until 2022 [29]. The tpm ligand, a neutral, strong six-electron donor *via* three nitrogen atoms (κ^3*N*), imparts substantial stability to the metal coordination set [30,31]. Complex [RuCl(tpm)(PPh$_3$)$_2$]Cl, **1**, a benchmark material in this chemistry, can be obtained through a straightforward two step-synthesis from commercially available ruthenium trichloride [32]. It can be further modified by replacing one PPh$_3$ ligand with a variety of ligands, enabling the tuning of physicochemical and biological properties. *In vitro* studies in 2D and 3D cancer cell models have identified **1**, and some of its derivatives, as promising anticancer drug candidates [32], with a mode of action predominantly localized in the mitochondria and linked to the disruption of calcium intake.

To enhance the anticancer activity of metal complexes, a widely

* Corresponding authors.
E-mail addresses: sgou@seu.edu.cn (S. Gou), fabio.marchetti@unipi.it (F. Marchetti).
[1] These authors contributed equally to this work.

https://doi.org/10.1016/j.jinorgbio.2024.112703
Received 29 April 2024; Received in revised form 17 July 2024; Accepted 15 August 2024
Available online 17 August 2024

investigated approach involves coupling a metal structure with documented anticancer activity to a bioactive organic molecule expected to exert complementary biological functions [33–35]. This strategy has aroused interest in various ruthenium complexes [36–39], and we demonstrated its successful application to ruthenium-tpm compounds derived from **1** and functionalized with NSAIDs (non-steroidal anti-inflammatory drugs) or ethacrynic acid [40].

We hypothesized that conjugating the {RuCl(tpm)(PPh_3)} scaffold with a fragment capable of interacting with DNA could be advantageous, expanding the mode of action of the resulting complex. Chlorambucil (**CA**), an established orally administered drug against lymphoma and chronic lymphocytic leukemia, acts as an alkylating agent through a multitargeted mechanism, with DNA crosslinking proposed as predominant [41,42]. Interestingly, modifying the chlorambucil skeleton with suitable fragments may provide significant effects to its biological activity, including anti-angiogenic properties [43]. Moreover, the incorporation of chlorambucil has been reported to enhance the *in vitro* antitumor efficacy of ruthenium(II) arene [44], platinum(IV) [45] and diiron(I) complexes [46].

In this work, we present the synthesis of a new chlorambucil-pyridine ligand, and its coordination to ruthenium-tpm. The functionalized pyridine ligand and the resulting complex underwent extensive investigation to assess their antitumor activity. Additionally, two {Ru^{II}-tpm}-pyridine complexes lacking chlorambucil were included in this study for comparison as relevant counterparts.

2. Results and discussion

2.1. Synthesis and structural characterization of compounds

The esterification of chlorambucil with 4-pyridinemethanol ($\mathbf{Py^{OH}}$) was carried out in dichloromethane at room temperature, using the Steglich protocol [47]. The resulting product, $\mathbf{Py^{CA}}$, was isolated in 75% yield after purification through silica chromatography (Scheme 1A). Subsequently, the 4-substituted pyridines $\mathbf{Py^{CA}}$, $\mathbf{Py^{NH2}}$ (4-amino-pyridine) and $\mathbf{Py^{OH}}$ (a potential hydrolysis product of $\mathbf{Py^{CA}}$) were utilized as ligands towards the {RuCl(PPh_3)(tpm)} scaffold (Scheme 1B).

The reactions of the bis-triphenylphosphine complex **1** with the chlorambucil-decorated pyridine $\mathbf{Py^{CA}}$ and 4-aminopyridine ($\mathbf{Py^{NH2}}$) were conducted in 2-propanol and ethanol, respectively, at reflux temperature. The resulting new complexes **2** and **3** were isolated in approximately 90% yields after work-up. Compound **4** was prepared similarly, following the literature procedure [40].

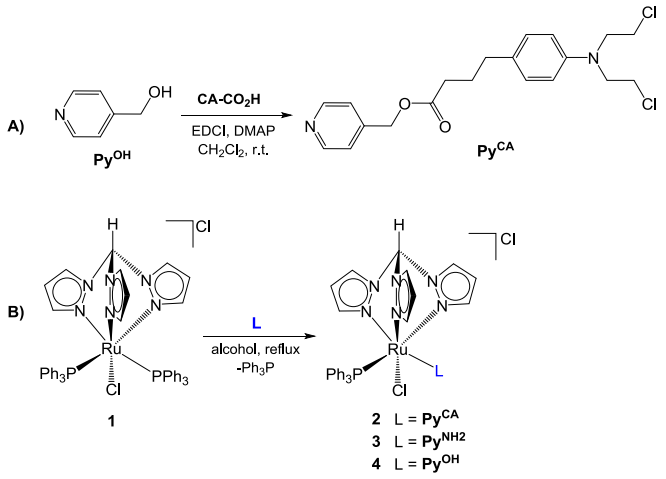

Scheme 1. A) Synthesis of chlorambucil-derivatized pyridine. EDCI = 1-ethyl-3-(3-dimethylaminopropyl)carbodiimide; DMAP = 4-pyridinemethanol. B) Synthesis of ruthenium(II) tris(pyrazolyl)methane complexes containing pyridine ligands.

The IR spectrum of **3** (solid state) displays an absorption peak related to the ester group at 1736 cm^{-1}, close to the value of 1728 cm^{-1} observed for $\mathbf{Py^{CA}}$. On the other hand, a diagnostic signal in the IR spectrum of **4** is provided by the N—H stretching band, occurring at 3325 cm^{-1}. The NMR spectra of **2–3** display single sets of resonances. The ^{31}P signal is observed at 50.4 ppm in both complexes, whereas it was detected at 40.1 ppm in the precursor **1**. This data highlights a significant electronic effect resulting from PPh_3/pyridine substitution (Scheme 1B) but suggests that peripheral variations in the pyridine ligand have a minor impact on the remaining PPh_3 ligand. In the ^1H and ^{13}C spectra of **2**, the signal related to $\mathbf{Py^{CA}}$ undergoes a negligible shift compared to uncoordinated $\mathbf{Py^{CA}}$, except for the CH units adjacent to the pyridine nitrogen. Specifically, these ^1H and ^{13}C resonances fall at 8.09 and 156.7 in **2** and at 8.77 and 150.4 in $\mathbf{Py^{CA}}$.

The structure of **3** was confirmed by single crystal X-ray diffraction (Fig. 1). The Ru center displays a distorted octahedral coordination, being bonded to a tridentate tpm, a chloride, a PPh_3 and a *p*-amino-pyridine ligand. All bonding parameters are comparable to those previously reported for related [RuCl(κ^3-tpm)(PPh_3)(L)]Cl complexes (L = aromatic N-donor ligand) [32,40]. Compound **3** crystallizes as the solvate **3**·Et_2O·$2H_2O$, that contains H-bonds involving the NH_2-group of the *p*-amino-pyridine ligand as donor and the Et_2O [N(8)-H(82) 0.88(2) Å, H(82)···O(51)#1 2.30(3) Å, N(8)···O(51)#1 3.147(5) Å, <N(8)H(82)O(51)#1163(5)°; symmetry operation #1 x + 1, y, z] and H_2O molecules [N(8)-H(81) 0.88(2) Å, H(82)···O(101)#1 2.17(2) Å, N(8)···O(101)#1 3.034(5) Å, <N(8)H(81)O(101)#1167(5)°] as acceptors.

2.2. Solubility, partition coefficients and stability in aqueous media

The behavior in aqueous solutions of the new compounds $\mathbf{Py^{CA}}$, **2** and **3** was evaluated by spectroscopic methods, and the results are compiled in Table 1. The solubility was measured in saturated D_2O solution at ambient temperature, using ^1H NMR spectroscopy and dimethyl sulfone (Me_2SO_2) as the internal standard. Octanol-water partition coefficients (Log P_{ow}) were determined by a UV–Vis method (see Experimental for details) [48]. The water solubility of **3** resembles that of the previously reported pyridine-methanol complex **4**, and the Log P_{ow} value of **3**, likewise **4**, indicates substantial amphiphilicity. In

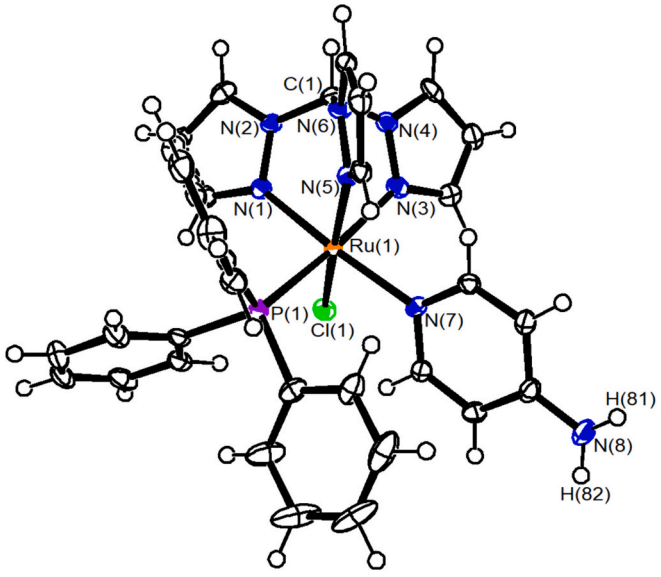

Fig. 1. View of the molecular structure of **3**. Displacement ellipsoids are at the 50% probability level. Selected bond lengths (Å) and angles (°): Ru(1)-N(1) 2.056(3), Ru(1)-N(3) 2.104(3), Ru(1)-N(5) 2.093(3), Ru(1)-N(7) 2.095(3), Ru(1)-P(1) 2.3186(11), Ru(1)-Cl(1) 2.4165(11), N(1)-Ru(1)-N(3) 85.56(14), N(1)-Ru(1)-N(5) 87.63(14), N(3)-Ru(1)-N(5) 82.44(13), P(1)-Ru(1)-N(7) 93.82(9), P(1)-Ru(1)-Cl(1) 98.71(4), N(7)-Ru(1)-Cl(1) 88.59(9).

Table 1
Solubility in D_2O at 21 °C; octanol/water partition coefficient (Log P_{ow}); assessment of stability of compounds in aqueous (D_2O, for **3** and **4**; DMSO-d_6/D_2O/ 4:1 *v*/v, for **2** and **Py^{CA}**) or in cell culture medium (DMEM-d, for **3** and **4**; DMEM-d/DMSO-d_6 4:1 v/v, for **2** and **Py^{CA}**) solution at 37 °C. [a]Calculated by ^{1}H NMR using dimethylsulfone (Me_2SO_2) as internal standard. [b]Data from the literature [ref. 40].

Compound	Solubility / 10^{-3} mol•L^{-1} [a]	Log P_{ow}	Residual % in aqueous solution (48 h) [a]	Residual % in DMEM culture medium (24 h) [a]
Py^{CA}	$< 1•10^{-4}$	> 2	72	99
2	$< 1•10^{-4}$	> 2	72	90
3	1.9	−0.11 ± 0.14	99	79
4 [b]	2.3	−0.25 ± 0.04	99	96

contrast, the hydrophobic character of the chlorambucil moiety within **Py^{CA}** and **2** results in lower solubility and pronounced lipophilicity of these compounds, with both solubility and Log P_{ow} values exceeding the quantitation threshold of the respective techniques.

Next, the speciation of **Py^{CA}**, **2** and **3**, in D_2O solutions maintained at 37 °C, was monitored over 48 h by ^{1}H and ^{31}P NMR spectroscopy; the solutions with **2** and **Py^{CA}** were diluted with DMSO-d_6 to achieve appreciable solubility. Thus, **Py^{CA}** in DMSO-d_6/D_2O undergoes partial hydrolysis (28%) of the -CH_2Cl units within the chlorambucil fragment, as suggested by the appearance of new signals in the aromatic region and for such CH_2. This process was previously observed for chlorambucil in aqueous solution [46]. The same chloride/hydroxide exchange also occurs in **2**, but to a lower extent (6%). Additionally, **2** is subjected to slow and progressive substitution of the **Py^{CA}** ligand by dimethylsulfoxide (22%) [49], as evidenced by the appearance of a distinct signal at 38.3 ppm in the ^{31}P NMR spectrum. Collected data do not evidence the formation of **CA** from **2**. On the other hand, **3** and **4** underwent negligible degradation in D_2O after 48 h at 37 °C.

The stability of the compounds was also assessed in a cell culture medium (DMEM) over 24 h, revealing a general, substantial robustness in this physiological-like medium.

3. Biological studies

3.1. Cytotoxicity

The cytotoxicity of compounds **Py^{CA}**, **2**, **3** and **4** was evaluated against various cancer cell lines, including MCF-7 (breast cancer), HCT116 (colon cancer), Hela (cervical cancer), A2780 (ovarian cancer) and A2780-cisR (cisplatin-resistant ovarian cancer), as well as the human normal liver cell line L02. Cisplatin and chlorambucil served as positive controls. As shown in Table 2, the ruthenium complexes **2–4** demonstrated cytotoxic effects on the tested cancer cell lines comparable to those of cisplatin, while the ligand **Py^{CA}** exhibited anticancer activity substantially analogous to that of its parent molecule chlorambucil. Notably, the activity of the chlorambucil-decorated ruthenium complex **2** is significantly higher than the distinct ones of chlorambucil and **Py^{CA}** towards the tested cancer cell lines. In particular, **2** showed the most potent antiproliferative activity against Hela cells, with an IC_{50} value of 6.7 μM, outperforming cisplatin (9.3 μM) and chlorambucil (26 μM). Furthermore, the performance of **2** is slightly higher when compared to the chlorambucil-lacking ruthenium complexes **3** and **4**. To further evidence synergistic effects, we tested a 1:1 M combination of the pyridine complex **4** and chlorambucil on Hela cancer cells. The resulting IC_{50} value was significantly lower than those related to the distinct compounds, and lower than that of the conjugated complex **2**, comprising the chlorambucil fragment chemically ligated to the pyridine ligand. These findings highlight the occurrence of synergistic effects provided by the two components, *i.e.* the ruthenium-pyridine structure and chlorambucil, especially when chemically combined in **2**.

As expected, cisplatin exhibited weak antitumor efficacy against the A2780/cis-R cell line due to drug resistance, with an activity approximately four-fold lower with respect to A2780 cells. Significantly, both **2** and **4** maintained sensitivity to cisplatin-resistant A2780/cis-R cells similar to what observed in A2780 cells, with resistance factors (RF) values <2.0. Both complexes exhibited stronger cytotoxicity in the resistant cells than cisplatin. All the investigated compounds, including cisplatin, did not demonstrate an appreciable selectivity against the cancer cell lines compared to the noncancer L02 cell line.

Based on the preliminary cytotoxicity results, complex **2** and its chlorambucil-lacking counterpart **4** were selected for further studies.

3.2. Cell uptake of ruthenium

The extent of ruthenium uptake was determined using ICP-MS technique, after incubating the selected compounds in Hela cells for 12 h. As shown in Table 3, the amount of ruthenium detected for complex **2** was substantially higher than for complexes **3** and **4**, consistent with the related Log P_{ow} values (Table 1). Moreover, determination of the intracellular distribution indicates a prevalent accumulation of ruthenium in the cell nucleus.

Table 3
Ruthenium uptake in Hela cancer cells after 12 h exposure to selected complexes, and intracellular distribution.

Complex (10 μM)	Ru (ng/10^6 cells)	Nuclei	Cytoplasm	Mitochondria
2	230 ± 20	109 ± 18	65 ± 9	35 ± 6
3	92 ± 13	37 ± 15	21 ± 4	10 ± 3
4	56 ± 5	18 ± 2	10.0 ± 1.3	5 ± 0.7

Table 2
Cytotoxic effects of **2**, **3**, **4**, **Py^{CA}**, cisplatin and chlorambucil against human cancer (MCF-7, HCT116, Hela, A2780 and A2780/cisR) and human normal (L02) cell lines.

Compound	IC_{50} (μM)[a]						
	L02	MCF-7	HCT-116	Hela	A2780	A2780-cisR	RF[b]
2	13.3 ± 1.4	11.7 ± 1.1	10.9 ± 1.0	6.7 ± 0.6	9.1 ± 0.8	15.1 ± 1.4	1.7
3	18 ± 2	9.4 ± 0.9	14.4 ± 1.4	12.8 ± 1.2	8.7 ± 0.8	23 ± 2	2.6
4	27 ± 2	17.5 ± 1.4	15.1 ± 1.4	18 ± 2	19 ± 2	21 ± 2	1.1
Py^{CA}	24 ± 2	20 ± 2	18 ± 2	18 ± 2	13.8 ± 1.2	33 ± 3	2.4
Cisplatin	11.0 ± 1.1	7.8 ± 0.7	16 ± 2	9.3 ± 0.9	5.7 ± 0.5	24 ± 2	4.2
Chlorambucil	35 ± 3	12.0 ± 1.2	12.9 ± 1.2	26 ± 3	15.2 ± 1.5	37 ± 4	2.4
4 + Chlorambucil				10.7 ± 0.5			

[a] IC_{50} refers to the dose required to inhibit 50% of the cells present in the control wells. The IC_{50} values reported are the average of at least three independent determinations.

[b] Resistance Factor (RF) is calculated as follows: RF value = IC_{50} (A2780/cisR)/IC_{50} (A2780).

3.3. Cell apoptosis

Apoptosis, an active cellular suicide behavior regulated by several genes, can be induced by anticancer agents. Apoptotic analysis of the selected compounds against Hela cells was conducted using the Annexin V-FITC/PI double staining method. Data in Fig. 2 indicate that complex **2** could induce a high apoptotic rate (approximately 27%). In contrast, the percentage of apoptotic cells was lower after incubation with **Py^{CA}**, **4** and chlorambucil, respectively (21%, 22% and 18%). Overall, it can be inferred that **2** is able to effectively induce cancer cell apoptosis.

3.4. Cell cycle arrest

To investigate whether the strong cytotoxicity exerted by complex **2** is attributable to cell cycle arrest, we analyzed cell cycle distributions in Hela cells using propidium iodide (PI) staining by flow cytometry. As depicted in Fig. 3, treatment with the ligand **Py^{CA}**, compared to control cells, resulted in a decrease in the percentage of cells in the G0/G1 and S phases from 64.17% to 54.84% and 13.34% to 10.01%, respectively. More importantly, incubation of Hela cells with **2** led to an increase in the percentage of cells in the S phase from 13.34% to 27.23%, whereas the percentage of cells in the G0/G1 and G2/M phases decreased from 64.17% to 55.77% and 22.49% to 17%, respectively. In contrast, chlorambucil exhibited a cell cycle profile somewhat similar to that of **Py^{CA}**. These results indicate that **2** primarily arrests the cell cycle at the S phase.

3.5. ROS production, mitochondrial membrane potential and western blotting assays

We employed the ROS fluorescent probe DCFH-DA to evaluate the ability of the investigated compounds to increase the total basal production of reactive oxygen species (ROS) in Hela cancer cells. The fluorescence intensity in Hela cells treated with complex **2** was notably higher compared to cells treated with **Py^{CA}**, **4**, or chlorambucil, pointing out that **2** is capable of generating a superior ROS response (Fig. 4A). Since ROS accumulation can induce oxidative damage to mitochondrial membrane potential (MMP), we assessed MMP in Hela cells treated with the compounds. Thus, we observed a significant decrease in MMP levels upon treatment with **2** compared to **Py^{CA}**, **4**, or chlorambucil (Fig. 4B).

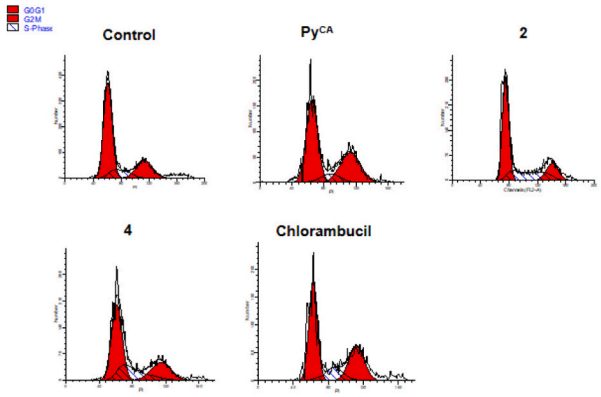

	G0/G1 (%)	S (%)	G2/M (%)
Control	64 ± 3	13 ± 1	23 ± 1
Py^{CA} (10 μM)	55 ± 3	10 ± 1	35 ± 2
2(10 μM)	56 ± 4	27 ± 1	17 ± 1
4 (10 μM)	53 ± 3	24 ± 1	23 ± 2
Chlorambucil (10 μM)	52 ± 2	15 ± 1	33 ± 2

Fig. 3. Cell cycle arrest effects of selected compounds (10 μM) on Hela cells after 24 h treatment.

Then, to elucidate the effects of the tested compounds on key proteins involved in the mitochondrial apoptotic pathway, namely caspase-3, p53, and Parp-1, we conducted western blotting assays. As depicted in Fig. 4C, both cleaved-caspase-3 and p53 levels were significantly elevated in **2**-treated group compared to treatment with **Py^{CA}**, **4** or chlorambucil, while the expression of Parp-1 decreased. These findings suggest that the ruthenium complex **2** may impact the mitochondrial apoptotic pathway, ultimately leading to cancer cell death.

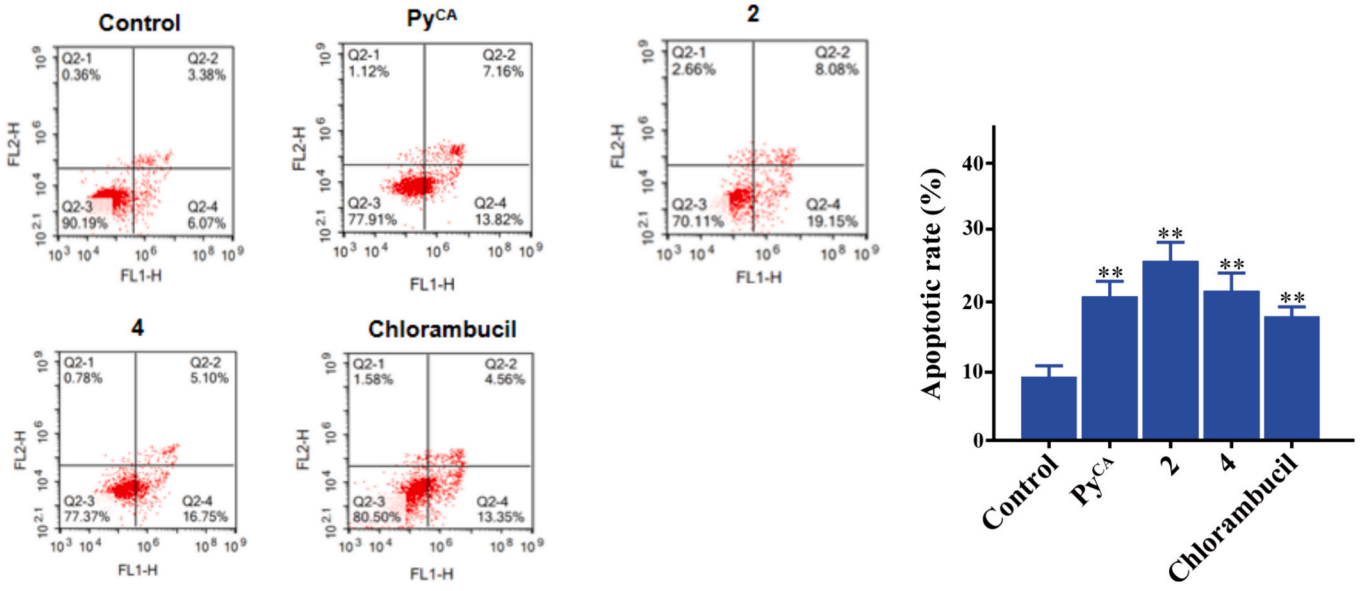

Fig. 2. Apoptotic effects of selected compounds at the concentration of 10 μM. Apoptotic rates were detected using the Annexin V-FITC/PI probe. The results represent at least three independent experiments, and the data are shown as the mean ± SD. *P* values were calculated using the student's *t*-tests (*$p < 0.05$, **$p < 0.01$ *versus* control ; $^{\#}p < 0.05$, $^{\#\#}p < 0.01$ *versus* the chlorambucil-treated group).

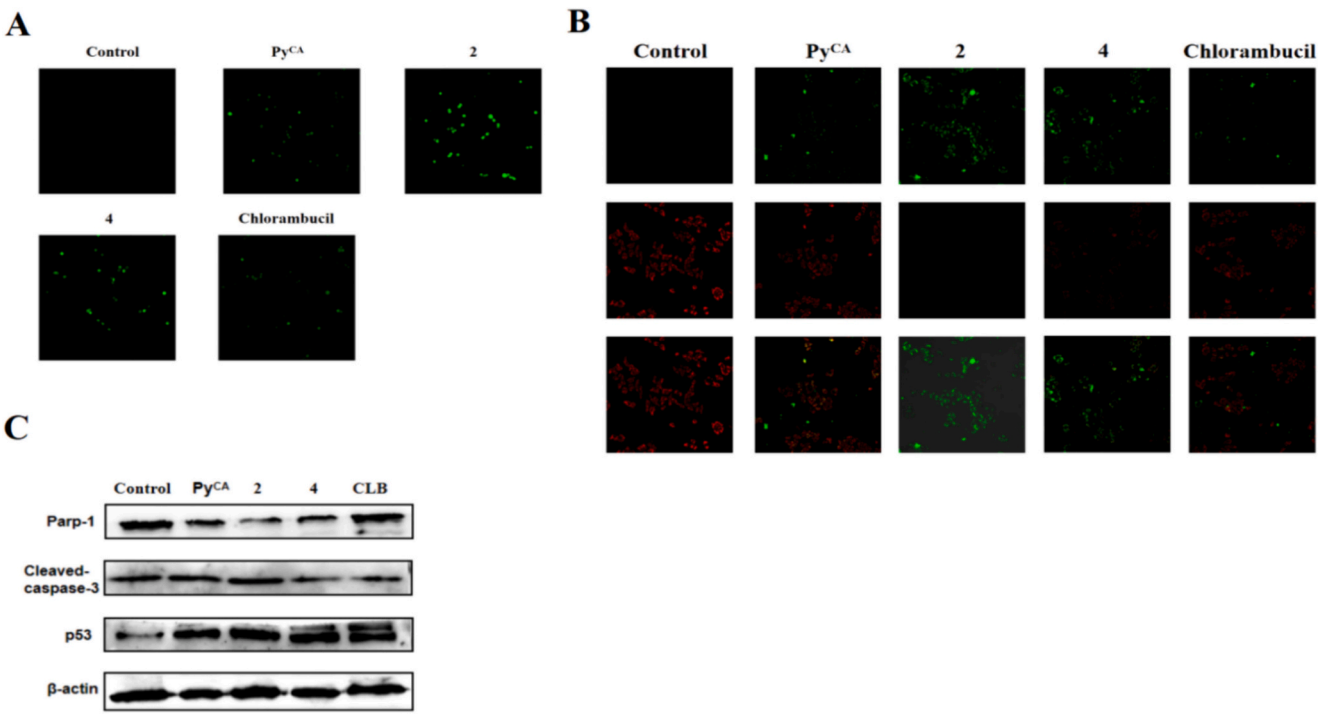

Fig. 4. (A) ROS and (B) MMP levels in Hela cells treated with the examined compounds. (C) Expression levels of Parp-1, cleaved-caspase-3 and p53 from Western blotting.

3.6. DNA damage

Since chlorambucil-based compounds could inhibit DNA and RNA synthesis, leading to cell apoptosis, the comet test was employed to assess the extent of DNA damage induced by the investigated compounds. Remarkably, complex **2** elicited prominent fluorescence tailing in Hela cells (Fig. 5). Moreover, the data indicated that the fluorescence tailing observed in Hela cells treated with **2** was significantly more pronounced and lasted longer compared to cells treated with **Py^{CA}**, **4** or chlorambucil. These findings suggest that **2** can induce substantial DNA damage in Hela cells, ascribable to the chlorambucil moiety apart from the ruthenium coordination unit.

As γ-H2AX is a crucial marker of DNA damage, immunofluorescence was used to measure the expression level of γ-H2AX and ascertain whether complex **2** induced higher levels of DNA damage. Remarkably, treatment with **2** led to a substantial increase in the fluorescence intensity of γ-H2AX in Hela cells compared to cells treated with **Py^{CA}** or chlorambucil (Fig. 6). These findings indicate that **2** significantly up-

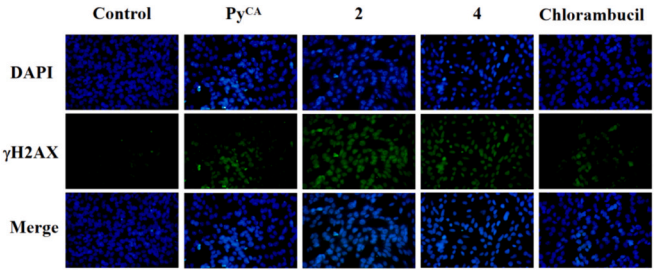

Fig. 6. The expression levels of γ-H2AX in Hela cells treated with the selected compounds as determined by immunofluorescence.

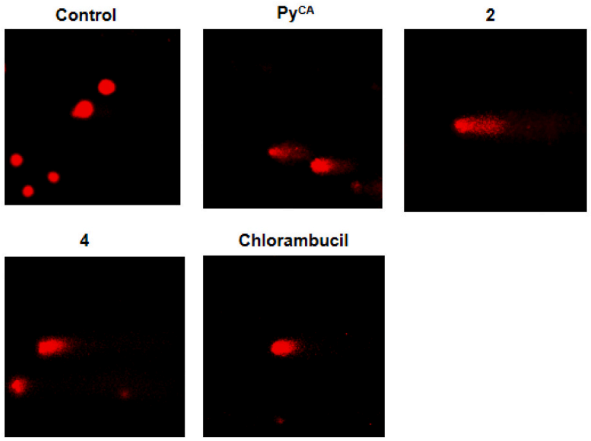

Compounds	head（%）	tail（%）
Control	97 ± 5	3 ± 0
Py^{CA}	75 ± 5	27 ± 1
2	59 ± 3	41 ± 3
4	80 ± 3	20 ± 1
Chlorambucil	86 ± 5	14 ± 0

Fig. 5. DNA damage levels and fluorescence tailing length of Hela cancer cells after treatment with the selected compounds (10 μM concentration).

regulated the expression of γ-H2AX, suggesting severe DNA damage induced by this compound.

4. Concluding remarks

We report the synthesis of a novel ruthenium structure incorporating the skeleton of chlorambucil, an anticancer drug known to exert its activity essentially through DNA damage. This complex (**2**) revealed an outstanding stability in a physiological-like solution, and a promising antiproliferative activity towards a panel of cancer cell lines, attributable to substantial lipophilicity facilitating cell membrane diffusion. The IC_{50} values evidence an improved performance compared to chlorambucil and analogous complexes lacking the chlorambucil moiety, or their combination, highlighting a slightly favorable effect provided by the ruthenium-chlorambucil chemical conjugation. Based on targeted experiments conducted on Hela cancer cells, the mode of action of **2** seems related to its ability to interfere with the mitochondrial activity through enhancement of ROS production and MMP decrease. Furthermore, data suggest that the chlorambucil moiety, when incorporated into complex **2**, retains its ability to behave as an alkylating agent. This property allows the metallic complex to induce DNA damage, leading to S-phase cell cycle arrest and ultimately triggering apoptosis in Hela cells. The reported results provide insights into the conjugation of a well-established anticancer drug with a robust ruthenium scaffold based on the tripodal tris-pyrazolylmethane ligand, which has been scarcely explored in medicinal chemistry. This synthetic approach paves the way for exploring new possibilities in the development of a novel class of metallodrugs for cancer therapy.

5. Experimental

5.1. Materials and methods

Reactants and solvents were purchased from Alfa Aesar, Merck, Strem or TCI Chemicals, and were of the highest purity available. EDCI•HCl was stored under N_2 at −20 °C as received. Tris(1-pyrazolyl) methane (tpm) [50] and complexes **1**[32] and **4**[40] were prepared according to literature procedures. Reactions were conducted under N_2 atmosphere using standard Schlenk techniques, and all products were stored in air once isolated. Dichloromethane, toluene, and diethyl ether were dried with the solvent purification system mBraun MB SPS5, while methanol was distilled from calcium hydride and isopropanol from magnesium. UV–Vis spectra (250–800 nm) were recorded on a Ultraspec 2100 Pro spectrophotometer using PMMA cuvettes (1 cm path length). IR spectra of solid samples were recorded on Agilent Cary630 FTIR spectrometer. IR spectra were processed with Spectragryph software [51]. NMR spectra of ruthenium complexes were recorded at 298 K on a Jeol JNM-ECZ500R instrument equipped with a Royal HFX Broadband probe, while NMR spectra of organic products were recorded at 298 K on Bruker spectrometer (400 MHz). Chemical shifts (expressed in parts per million) have been referenced to the residual solvent peaks (^{1}H, ^{13}C) [52] or to external standard (^{31}P to H_3PO_4). ^{1}H and ^{13}C{^{1}H} NMR spectra of ruthenium complexes were assigned with the assistance of ^{1}H—^{13}C (*gs*-HSQC and *gs*-HMBC) correlation experiments [53]. Elemental analyses (CHNS) were performed on a Vario MICRO cube instrument (Elementar). ESI-Q/ToF flow injection analyses (FIA) were conducted on a 1200 Infinity HPLC coupled to a Jet Stream ESI interface with a Quadrupole-Time of Flight tandem mass spectrometer 6530 Infinity Q-TOF (Agilent Technologies.

5.2. Synthesis and characterization of compounds

5.2.1. Pyridin-4-yl-methyl-2-(2,3-dichloro-4-(2-methylenebutanoyl) phenoxy)acetate, Py^{CA} (Chart 1)

A solution of 4-pyridinemethanol (140 mg, 1.28 mmol), chlorambucil (429 mg, 1.41 mmol), EDCI•HCl (294 mg, 1.54 mmol) and dimethyaminopyridine (DMAP; 30 mg, 0.26 mmol), in anhydrous dichloromethane (15 mL), was allowed to stir at room temperature for 16 h. Then the volatiles were evaporated under reduced pressure and the crude product purified by silica chromatography (hexane/Et_2O from 2:1 *v*/v to 1:1 v/v ratio). Colorless powder stored at −30 °C, yield 382 mg (75%). Anal. calcd. for $C_{20}H_{24}Cl_2N_2O_2$: C, 60.76; H, 6.12; N, 6.97. Found: C, 60.52; H, 6.16; N, 7.12. IR (solid state): $\tilde{\upsilon}$/cm^{-1} = 3027w, 3003w, 2966 m, 2942 m, 2930 m, 2914 m, 2902 m, 2884 m, 1728s ($\tilde{\upsilon}_{C=O}$), 1615 m, 1660 m, 1558w, 1519s, 1449w, 1429w, 1413 m, 1315 m, 1361 m, 1344 m, 1265 m, 1248 m, 1176s, 1140 m, 1086 m, 1065 m, 1010 m, 990 m, 917 m, 804 s, 744w, 117w, 648 m, 681w, 635w, 522w, 497 m, 477w, 445w, 426w. ^{1}H NMR (CD_2Cl_2): δ/ppm = 8.77 (d, 2H, $^3J_{HH}$ = 5.2 Hz, C^{1}H); 7.45 (d, 2H, $^3J_{HH}$ = 5.1 Hz, C^{2}H); 7.26 (d, 2H, $^3J_{HH}$ = 8.3 Hz, C^{10}H); 6.84 (d, 2H, $^3J_{HH}$ = 8.4 Hz, C^{11}H); 5.54 (s, 2H, C^{4}H); 3.88 (m, 8H, C^{14}H + C^{13}H); 2.77 (t, 2H, $^3J_{HH}$ = 7.6 Hz, C^{8}H); 2.62 (t, 2H, $^3J_{HH}$ = 7.5 Hz, C^{6}H); 2.13 (q, 2H, $^3J_{HH}$ = 7.5 Hz, C^{7}H). ^{13}C{^{1}H} NMR (CD_2Cl_2): δ/ppm = 173.3 (C^5); 150.4 (C^1); 145.6 (C^3); 145.0 (C^{12}); 130.9 (C^9); 130.0 (C^{20}); 122.2 (C^2); 112.7 (C^{11}); 64.5 (C^4); 53.9 (C^{13} or C^{14});41.2 (C^{13} or C^{14}); 34.3 (C^8); 33.8 (C^6); 27.2 (C^7).

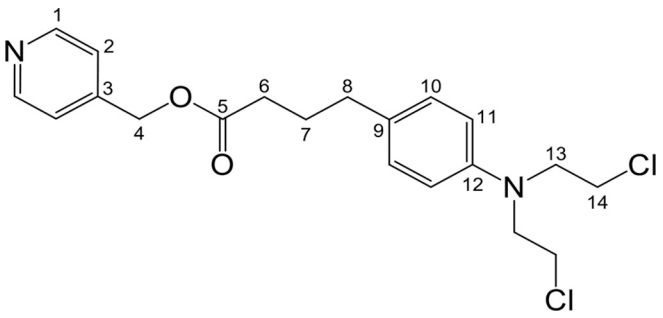

Chart 1. Structure of $\mathbf{Py^{CA}}$ (labelling refers to carbon atoms).

5.2.2. [RuCl(κ^3-tpm)(PPh$_3$)(Py^{CA})]Cl, 2 (Chart 2)

A solution of **1** (150 mg, 0.160 mmol) and $\mathbf{Py^{CA}}$ (117 mg, 0.297 mmol) in anhydrous 2-propanol (8 mL) was heated at reflux for a 8 h. After cooling to room temperature, the volatiles were evaporated under reduced pressure. The crude product was redissolved in the minimum volume of dichloromethane, precipitated with diethyl ether, filtered and dried under vacuum. Yellow solid, yield 148 mg (86%). Anal. calcd. for $C_{48}H_{49}Cl_4N_8O_2PRu$: C, 55.23; H, 4.73; N, 10.74. Found: C, 54.92; H, 4.80; N, 10.85. IR (solid state): $\tilde{\upsilon}$/cm^{-1} = 3103w, 3055w, 2960w, 2924w, 2869w, 1736 m ($\tilde{\upsilon}_{C=O}$), 1613 m, 1529 m, 1480w, 1449w, 1432 m, 1407 m, 1384w, 1351w, 1248 m, 1222w, 1181 m, 1142w, 1089s, 1053 m, 857 m, 791 s, 749 s, 695 s, 608w, 528 s, 511 m, 501 m, 456w, 424w. ^{1}H NMR (CD_2Cl_2): δ/ppm = 12.36 (s, 1H, C^{6}H); 9.03, 8.85, 8.77 (d, 3H, $^3J_{HH}$ = 2.8 Hz, C$^\gamma$H); 8.09 (s-br, 2H, C^{1}H); 7.35 (t, 3H, $^3J_{HH}$ = 7.8 Hz, C^{18}H); 7.30, 7.08 (d, 2H, $^3J_{HH}$ = 1.5 Hz, C$^\alpha$H); 7.18 (t, 6H, $^3J_{HH}$ = 7.6 Hz, C^{17}H); 7.06 (d, 2H, $^3J_{HH}$ = 8.3 Hz, C^{10}H); 6.97 (t, 6H, $^3J_{HH}$ = 8.8 Hz, C^{16}H); 6.86 (d, 2H, $^3J_{HH}$ = 6.02 Hz, C^{2}H); 6.65–6.63 (m, 3H, CHα + C^{11}H); 6.36, 6.16, 6.06 (t, 3H, $^3J_{HH}$ = 2.6 Hz, C$^\beta$H); 5.07 (s, 2H, C^{4}H); 3.72–3.61 (m, 8H, C^{14}H + C^{13}H); 2.56 (t, 2H, $^3J_{HH}$ = 7.5 Hz, C^{8}H); 2.41 (t, 2H, $^3J_{HH}$ = 7.5 Hz, C^{6}H); 1.92 (q, 2H, $^3J_{HH}$ = 7.5 Hz, C^{7}H). ^{13}C{^{1}H} NMR (CD_2Cl_2): δ/ppm = 173.1 (C^5); 156.7 (C^1); 149.1, 148.6, 144.5 (C$^\gamma$); 146.2 (C^3); 145.0 (C^{12}); 136.2, 135.3, 134.1 (C$^\alpha$); 134.5 (d, $^2J_{CP}$ = 9.5 Hz, C^{16}); 132.4 (d, $^1J_{CP}$ = 40.6 Hz, C^{15}); 130.7 (C^9); 130.3 (d, $^4J_{CP}$ = 2.2 Hz, C^{18}), 130.0 (C^{10}); 128.6 (d, $^3J_{CP}$ = 9.2 Hz, C^{17}); 122.2 (C^2); 112.7 (C^{11}); 108.7, 108.6, 108.7 (C$^\beta$); 74.7 (C$^\delta$); 63.7 (C^3); 53.8 (C^{14} o C^3); 41.2 (C^{14} o C^{13}); 34.3 (C^8); 33.8 (C^6); 27.9 (C^7). ^{31}P{^{1}H} NMR (CD_2Cl_2): δ/ppm = 50.4. HR-ESI-MS(+): *m/z* found 1009.1814 [M]$^+$, calcd. for $C_{48}H_{49}Cl_3N_8O_2PRu$ 1009.1814. The isotopic pattern fits well the calculated ones.

5.2.3. [RuCl(κ^3-tpm)(PPh$_3$)(Py^{NH2})]Cl, 3 (Chart 3)

A solution of **1** (100 mg, 0.110 mmol) and 4-aminopyridine ($\mathbf{Py^{NH2}}$;

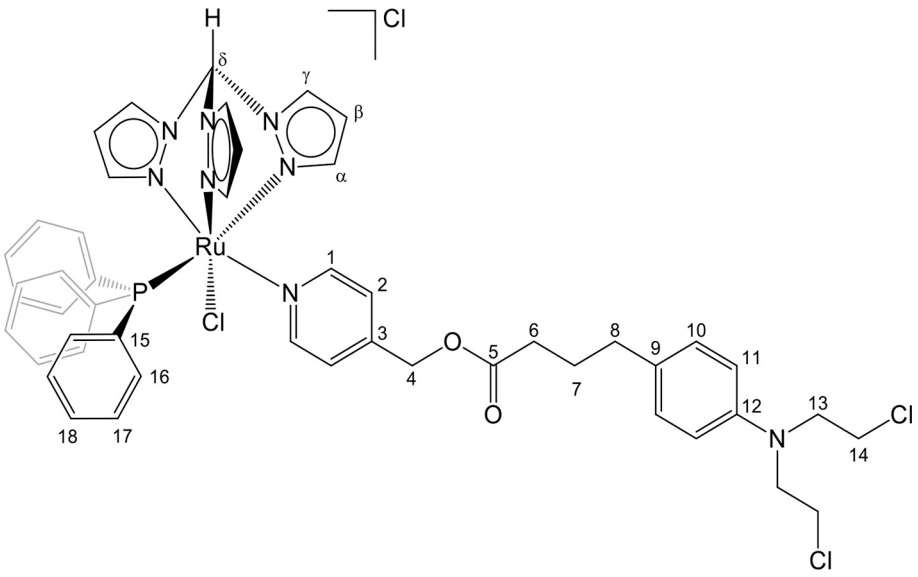

Chart 2. Structure of **2** (labelling refers to carbon atoms).

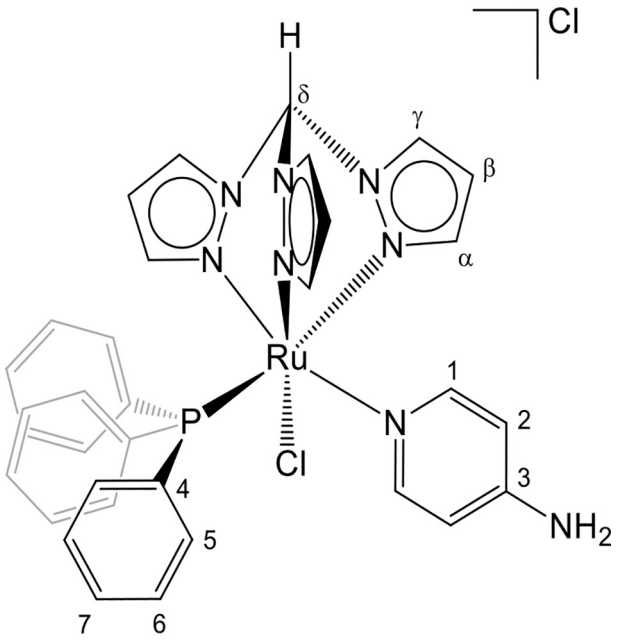

Chart 3. Structure of **3** (labelling refers to carbon atoms).

17 mg, 0.17 mmol) in ethanol (8 mL) was heated at reflux for a 16 h. After cooling to room temperature, the volatiles were evaporated under reduced pressure. The crude product was redissolved in the minimum volume of dichloromethane, precipitated with diethyl ether, filtered and dried under vacuum. Yellow solid, yield 76 mg (93%). Anal. calcd. For $C_{33}H_{31}Cl_2N_8PRu$: C, 53.37; H, 4.21; N, 15.09. Found: C, 53.73; H, 4.34; N, 14.87. IR (solid state): $\tilde{u}/cm^{-1}$ = 3325w ($\tilde{u}_{N\text{-}H}$), 3180w, 3103w, 2984w, 2969w, 2902w, 1628 m, 1514 m, 1480w, 1450w, 1433 m, 1410 m, 1288 m, 1284 m, 1252 m, 1211 m, 1089s, 1057s, 1027 m, 857 m, 791 m, 781 m, 458 m, 746 s, 696 s, 607w, 529 s, 504 s, 453w. ^{1}H NMR (CD_3OD): δ/ppm = 9.73 (s, 1H, $C^{\delta}H$); 8.51. 8.44, 8.44 (d-br, 3H, $C^{\gamma}H$); 7.51, 7.09, 6.89 (d-br, 3H, $C^{\alpha}H$); 7.43 (m, 5H, $C^7H + C^1H$); 7.25 (t, 6H, $^3J_{HH}$ = 7.7 Hz, C^5H); 7.02 (t, 6H, $^3J_{HH}$ = 8.7 Hz, C^6H); 6.58, 6.31, 6.24 (t-br, 3H, $C^{\beta}H$); 6.23 (m, 2H, C^2H). *NH_2 not observed.* $^{13}C\{^1H\}$ NMR (CD_3OD): δ/ppm = 156.5 (C3); 155.9 (br, C1); 150.8, 150.3, 146.3 (C^{α}); 136.5, 135.5, 134.2 (Cγ); 135.2 (d, $^3J_{CP}$ = 9.4 Hz, C^6); 133.7 (d, $^1J_{CP}$ = 40.4 Hz, C^4); 131.1 (d, $^4J_{CP}$ = 2.1 Hz, C^7); 129.3 (d, $^2J_{CP}$ = 9.1 Hz, C^5); 110.7 (C^2); 110.0, 109.6, 109.6 (C^{β}). $^{31}P\{^1H\}$ NMR (CD_3OD): δ/ppm = 52.6. ^{1}H NMR ($CDCl_3$): δ/ppm = 12.32 (s, 1H, $C^{\delta}H$); 9.07, 8.78, 8.70 (d, 3H, $^3J_{HH}$ = 2.9 Hz, $C^{\gamma}H$); 7.59 (s-br, 2H, C^1H); 7.43, 7.05, 6.58 (d, 3H, $^3J_{HH}$ = 2.2 Hz, $C^{\alpha}H$); 7.34 (t, 3H, C^7H); 7.18 (t, 6H, C^5H); 6.99 (t-br, 6H, C^6H); 6.32, 6.09, 6.00 (t, 3H, $^3J_{HH}$ = 2.9 Hz, $C^{\beta}H$); 6.19 (d, 2H, $^3J_{HH}$ = 2.28 Hz, C^2H); 4.42 (s-br, 2H, NH_2). $^{31}P\{^1H\}$ NMR ($CDCl_3$): δ/ppm = 50.4. Crystals suitable for X-ray diffraction were collected by slow evaporation of the solvent from a $CDCl_3$ solution of **3**. HR-ESI-MS(+): *m/z* found 707.1139 $[M]^+$, calcd. For $C_{33}H_{31}ClN_8PRu$ 707.1141. The isotopic pattern fits well the calculated one.

5.3. X-ray crystallography

Crystal data and collection details for **3**·Et_2O·$2H_2O$ are reported in Table 4. Data were recorded on a Bruker APEX II diffractometer

Table 4
Crystal data and measurement details for **3**·Et_2O·$2H_2O$.

	3·Et_2O·$2H_2O$
Formula	$C_{37}H_{45}Cl_2N_8O_3PRu$
FW	852.75
T, K	100(2)
λ, Å	0.71073
Crystal system	Triclinic
Space group	$P\bar{1}$
a, Å	10.2042(9)
b, Å	10.5007(9)
c, Å	18.8035(17)
α,°	98.529(3)
β,°	103.182(3)
γ,°	97.084(3)
Cell Volume, Å^3	1914.0(3)
Z	2
D_c, g•cm^{-3}	1.480
μ, mm^{-1}	0.639
F(000)	880
Crystal size, mm	0.19 × 0.13 × 0.08
θ limits,°	1.988–25.100
Reflections collected	20,773
Independent reflections	6794 [R_{int} = 0.0537]
Data / restraints /parameters	6794 / 117 / 524
Goodness on fit on F^2	1.138
R_1 ($I > 2\sigma(I)$)	0.0500
wR_2 (all data)	0.1096
Largest diff. Peak and hole, e Å^{-3}	0.997 / –0.788

equipped with a PHOTON2 detector using Mo–Kα radiation. Data were corrected for Lorentz polarization and absorption effects (empirical absorption correction SADABS) [54]. The structure was solved by direct methods and refined by full-matrix least-squares based on all data using F^2 [55]. Hydrogen atoms were fixed at calculated positions and refined by a riding model, except those bonded to N and O atoms, that have been located in the Fourier map and refined isotropically with retrained N-H and O—H distances. All non-hydrogen atoms were refined with anisotropic displacement parameters.

6. Behavior in aqueous media

a) Solubility in water. A suspension of the selected compound (3–5 mg) in a D_2O solution (0.7 mL) of Me_2SO_2 ($3.36{\cdot}10^{-3}$ M), was vigorously stirred at 21 °C for 3 h. The resulting saturated solution was then filtered over celite, transferred into an NMR tube and analyzed by ^{1}H NMR spectroscopy (delay time = 3 s; number of scans = 20). The concentration (solubility) was calculated by the relative integral (starting complex + aquo-complex) with respect to Me_2SO_2 (δ/ppm = 3.14). Results are compiled in Table 1.

b) Octanol/water partition coefficients (Log P_{ow}). Partition coefficients (P_{ow}; IUPAC: K_D partition constant [56]), defined as $P_{ow} = c_{org}/c_{aq}$, where c_{org} and c_{aq} are molar concentrations of the selected compound in the organic and aqueous phase, respectively, were determined by the shake-flask method and UV–Vis measurements [48,57,58]. Deionized water and 1-octanol were vigorously stirred for 24 h, to enable saturation of both phases, then separated by centrifugation.

A stock solution of complex **3** (*ca.* 2 mg) was prepared by first adding DMSO, (50 μL, to help solubilization), followed by octanol-saturated water (2.5 mL). The solution was diluted with octanol-saturated water (*ca.* 1:3 *v/v* ratio, $c_{Ru} \approx 10^{-4}$ M, so that $1.5 \leq A \leq 2.0$ at λ_{max}) and its UV–Vis spectrum was recorded (A^0_{aq}). An aliquot of the solution (V_{aq} = 1.2 mL) was transferred into a test tube and water-saturated octanol ($V_{org} = V_{aq} = 1.2$ mL) was added. The mixture was vigorously stirred for 20 min at 21 °C then centrifuged (5000 rpm, 5 min). The UV–Vis spectrum of the aqueous phase was recorded (A^f_{aq}) and the partition coefficient was calculated as $P_{ow} = (A^0_{aq} - A^f_{aq})/A^f_{aq}$ where A^0_{aq} and A^f_{aq} are the absorbance in the aqueous phase before and after partition with the organic phase, respectively.[57c]

For **2** and **Py^{CA}**, an inverse procedure was followed, starting from a solution of the compound in water-saturated octanol. The partition coefficient was calculated as $P_{ow} = A^f_{org}/(A^0_{org} - A^f_{org})$ where A^0_{org} and A^f_{org} are the absorbance in the organic phase before and after partition with the aqueous phase, respectively. The wavelength of the maximum absorption of each compound (280–380 nm range) was used for UV–Vis quantitation. The procedure was repeated three times for each sample (from the same stock solution); results are given as mean ± standard deviation (Table 1). Naphthoquinone was used as a reference compound (Log P_{ow} = 1.8 ± 0.2; literature: 1.71 [59]).

c) Stability in D_2O and DMSO-d_6/D_2O. The same sample of complex **3** as prepared at point a) was used in this experiment. In addition, **2** and **Py^{CA}** (2 mg) were dissolved in DMSO-d_6/D_2O 4:1 *v*/v solution (0.75 mL) containing Me_2SO_2 as standard [60]. The resulting solutions were stirred at 21 °C for 5 min, filtered over celite, transferred into an NMR tube, analyzed by ^{1}H NMR and ^{31}P NMR spectroscopy (delay time = 3 s; number of scans = 20) and then maintained at 37 °C for 48 h. After cooling to room temperature, NMR analyses were repeated. The percentage of starting compound (and related aquo complex, in the cases of **2** and **3**) was calculated by signal integrations with respect to Me_2SO_2 (c = $3.3{\cdot}10^{-3}$ mol•L^{-1}; δ/ppm = 3.14 in D_2O; δ/ppm = 2.95 in DMSO-d_6/D_2O 4:1 v/v; see Table 1 and Table S1).

d) Stability in cell culture medium. Powdered DMEM cell culture medium (1000 mg/L glucose and L-glutamine, without sodium bicarbonate and phenol red; D2902 - Merck) was dissolved in D_2O (10 mg/mL), according to the manufacturer's instructions. The solution of deuterated cell culture medium ("DMEM-d") was treated with Me_2SO_2 ($6.6{\cdot}10^{-3}$ M) and NaH_2PO_4 / Na_2HPO_4 (0.15 M, pD = 7.5 [61]), then stored at 4 °C under N_2. The same procedure reported at point c) was followed for the preparation and analysis of the samples, using DMEM-d instead of D_2O. The percentages of starting complex and related aquo complex were calculated by signal integrations with respect to Me_2SO_2 (δ/ppm = 3.16 in DMSO-d_6/DMEM-d 1:4 and 1:3 v/v; δ/ppm = 2.95 in DMSO-d_6/DMEM-d 4:1 *v*/v).

7. Biological studies

7.1. Cytotoxicity

The MCF-7, HCT-116, Hela, A2780 and A2780/cisR cancer cells (maintained in RPMI DMEM or RPMI1640 medium with 10% FBS at 37 °C under a humidified atmosphere of 5% CO_2) were seeded in 96-well plate at a concentration of 1×10^3 - 1×10^4 cells/well at 37 °C for 24 h. Subsequently, the medium containing distinct concentrations of **Py^{CA}**, **2**, **3**, **4,** chlorambucil in DMSO or cisplatin in H_2O was added, followed by further incubation for 72 h. Afterward, 10 μL of MTT (5 mg/mL) was supplemented to each well and incubated in dark for 4 h. The absorbance was measured at 490 nm using a microplate reader, and the IC_{50} values were determined using SPSS software. The use of *N,N*-dimethylformamide (DMF) as a solvent in the place of DMSO for selected compounds led to comparable IC_{50} values (μM) in Hela cells (see also Table 2): complex **2**, 6.7 ± 0.6 (DMSO) and 6.8 ± 0.3 (DMF); chlorambucil, 26 ± 3 (DMSO) and 25 ± 3 (DMF); mixture **4** + chlorambucil, 10.7 ± 0.5 (DMSO) and 10.2 ± 0.9 (DMF).

7.2. Cell apoptotic assay

Hela cells were cultured in 6-well plates until reaching 70% confluency. The cells were treated with 10 μM of the tested compounds for 24 h. After treatment, the cells were collected and stained with 5 μL Annexin V-FITC and 5 μL PI for 30 min in the dark. The data were obtained using flow cytometry.

7.3. Cell cycle assay

Cells were plated in 6-well plates and allowed to adhere overnight. After the overnight incubation, Hela cells were treated with 10 μM of the tested compounds in fresh cell culture medium for 24 h. Following the treatments, the cells were harvested, washed with PBS, and fixed with 75% cold ethanol at 4 °C overnight. Then, the cells were isolated by centrifugation and stained with PI dye for 30 min. Finally, the cells were analyzed using flow cytometry.

7.4. Comet assay

After treatment with 10 μM of the tested compounds for 12 h, the Hela cells were mixed with molten LM Agarose (Trevigen) at a ratio of 1:10 (*v*/v). The mixture was then dripped onto Comet Slide (Trevigen) and allowed to fix at 4 °C for 20 min. Subsequently, the cells were lysed at 4 °C for 1 h and immersed in a basic electrophoretic buffer at room temperature for 20 min. Following electrophoresis at 25 V for 30 min, the slides were washed with 0.4 mM Tris-HCl (pH 7.5), dried, stained with PI, and imaged using a fluorescence confocal microscope.

7.5. Western blot assay

Cells were plated and allowed to grow to 70% confluence before being treated with 10 μM of the tested compounds for 12 h. After treatment, the cells were lysed at 4 °C using a cell lysis buffer for 1 h, followed by centrifugating at 13000 rpm for 30 min at 4 °C. The supernatants were collected and quantified by the BCA protein assay kit. The corresponding protein was separated by SDS-PAGE on 10–15% gels and transferred onto polyvinylidene difluoride membranes. The

membranes were then probed with primary (1:1000) and secondary antibodies (1:2000). After three washes, the protein bands were visualized using a chemiluminescence reagent, and the labeled proteins were detected using an automatic chemiluminescence imaging analysis system.

7.6. Cell uptake assay

Cells were seeded in 6-well plates and incubated with 10 μM of the selected ruthenium complex in DMSO for 12 h. After treatment, the cells were harvested and washed with ice-cold PBS. The intracellular distributions of ruthenium in nucleus, cytoplasm and mitochondria were extracted using commercial kits according to the manufacturer's instructions. Subsequently, Hela cells and intracellular distributions were digested at 65 °C in 1 mL of 65% HNO_3 for 12 h. The amount of ruthenium in the cells of each sample was measured by ICP-MS.

7.7. Intracellular ROS detection

The ROS levels induced by the tested compounds were measured using the DCFH-DA assay kit (KeyGen Biotech, China). Cells were seeded in 6-well plates and treated with the compounds for 24 h. Then, the cells were incubated with 10 mM DCFH-DA probe for 30 min. Finally, the cells were harvested, resuspended in PBS, and stained. Flow cytometry was then employed to detect and analyze the stained cells, with data analysis performed using Flowjo Software.

7.8. Mitochondria membrane potential (MMP) assay

The cells were seeded in 6-well plates and treated with the tested compounds. After treatment, the JC-1 MMP Assay Kit (KeyGen Biotech, China) was used to detect MMP according to the manufacturer's instructions.

7.9. Immunofluorescence assay

The Hela cancer cells were grown on slides in 6-well plates and treated with the tested compounds for 24 h. Subsequently, the cells were incubated in a constant temperature incubator for 12 h. After removing the medium and washing with PBS, the cells were fixed with 1 mL of 4% paraformaldehyde solution for 20 min. Then, 1 mL of 0.5% Triton X-100 (KeyGen Biotech, China) was added for cell permeabilization for 30 min. After washing with PBS, the cells were blocked with FBS for 1 h. Following this, primary antibodies (diluted 1:100) were added for overnight incubation at 4 °C. The primary antibodies were washed off with PBS, and tetramethylrhodamine (TRITC)-labeled secondary antibody (diluted 1:1000) was added for 2 h. The cells were then stained with 4′,6-diamidino-2-phenylindole (DAPI) (diluted 1:1000, KeyGen Biotech, China) for 10 min. Fluorescence images were captured using a confocal microscope and analyzed using ImageJ software.

CRediT authorship contribution statement

Alberto Gobbo: Visualization, Validation, Resources, Methodology, Investigation, Formal analysis, Data curation, Conceptualization. **Feihong Chen:** Visualization, Validation, Methodology, Investigation, Formal analysis, Data curation, Conceptualization. **Stefano Zacchini:** Writing – original draft, Visualization, Validation, Software, Methodology, Investigation, Formal analysis, Data curation, Conceptualization. **Shaohua Gou:** Writing – review & editing, Writing – original draft, Visualization, Validation, Supervision, Software, Resources, Project administration, Methodology, Investigation, Funding acquisition, Formal analysis, Data curation, Conceptualization. **Fabio Marchetti:** Writing – review & editing, Writing – original draft, Visualization, Validation, Supervision, Software, Resources, Project administration, Methodology, Investigation, Funding acquisition, Formal analysis, Data curation, Conceptualization.

Declaration of competing interest

The authors declare no competing financial interests.

Data availability

No data was used for the research described in the article.

Acknowledgements

We thank the University of Pisa (Fondi di Ateneo 2022) and the National Natural Science Foundation of China (22077015 and 82173852) for financial support.

Appendix A. Supplementary data

IR and NMR spectra of ruthenium complexes. CCDC reference number 2346679 (**3**) contains the supplementary crystallographic data for the X-ray study reported in this work. This data is available free of charge at http://www.ccdc.cam.ac.uk/structures. Supplementary data to this article can be found online at [https://doi.org/10.1016/j.jinorgbio.2024.112703].

References

[1] E.J. Anthony, E.M. Bolitho, H.E. Bridgewater, O.W.L. Carter, J.M. Donnelly, C. Imberti, E.C. Lant, F. Lermyte, R.J. Needham, M. Palau, P.J. Sadler, H. Shi, F.-X. Wang, W.-Y. Zhang, Z. Zhang, Metallodrugs are unique: opportunities and challenges of discovery and development, Chem. Sci. 11 (2020) 12888–12917.
[2] E. Boros, P.J. Dyson, G. Gasser, Classification of metal-based drugs according to their mechanisms of action, Chem 6 (2020) 41–60.
[3] K.L. Haas, K.J. Franz, Application of metal coordination chemistry to explore and manipulate cell biology, Chem. Rev. 109 (2009) 4921–4960.
[4] R. Oun, Y.E. Moussa, N.J. Wheate, The side effects of platinum-based chemotherapy drugs: a review for chemists, Dalton Trans. 47 (2018) 6645–6653.
[5] L. Qi, Q. Luo, Y. Zhang, F. Jia, Y. Zhao, F. Wang, Advances in toxicological research of the anticancer drug cisplatin, Chem. Res. Toxicol. 32 (2019) 1469–1486.
[6] K. Peng, B.-B. Liang, W. Liu, Z.-W. Mao, What blocks more anticancer platinum complexes from experiment to clinic: major problems and potential strategies from drug design perspectives, Coord. Chem. Rev. 449 (2021) 214210.
[7] S. Ghosh, Cisplatin: the first metal based anticancer drug, Bioorg. Chem. 88 (2019) 102925.
[8] S. Dilruba, G.V. Kalayda, Platinum-based drugs: past, present and future, Cancer Chemother. Pharmacol. 77 (2016) 1103–1124.
[9] M. Marloye, G. Berger, M. Gelbcke, A survey of the mechanisms of action of anticancer transition metal complexes, Future Med. Chem. 8 (2016) 2263–2286.
[10] S. Thota, D.A. Rodrigues, D.C. Crans, E.J. Barreiro, Ru(II) compounds: next-generation anticancer metallotherapeutics? J. Med. Chem. 61 (2018) 5805–5821.
[11] S.M. Meier-Menches, C. Gerner, W. Berger, C.G. Hartinger, B.K. Keppler, Structure–activity relationships for ruthenium and osmium anticancer agents – towards clinical development, Chem. Soc. Rev. 47 (2018) 909–928.
[12] L. Zeng, P. Gupta, Y. Chen, E. Wang, L. Ji, H. Chao, Z.-S. Chen, The development of anticancer ruthenium(II) complexes: from single molecule compounds to nanomaterials, Chem. Soc. Rev. 46 (2017) 5771–5804.
[13] G. Bresciani, S. Boni, T. Funaioli, S. Zacchini, G. Pampaloni, N. Busto, T. Biver, F. Marchetti, Adding diversity to a diruthenium biscyclopentadienyl scaffold via alkyne incorporation: synthesis and biological studies, Inorg. Chem. 62 (2023) 12453–12467.
[14] F. Marszaukowski, I.D. Lao Guimarães, J.P. da Silva, L.H. da Silveira Lacerda, S. R. de Lazaro, M.P. de Araujo, P. Castellen, T. Toyomi Tominaga, R.T. Boeré, K. Wohnrath, Ruthenium(II)-arene complexes with monodentate aminopyridine ligands: insights into redox stability and electronic structures and biological activity, J. Organomet. Chem. 881 (2019) 66–78.
[15] P.J. Dyson, Ruthenium – a non-essential element that may become essential in treating chemoresistant cancers, Chimia 73 (2019) 332–333.
[16] E. Alessio, Thirty years of the drug candidate NAMI-A and the myths in the field of ruthenium anticancer compounds: a personal perspective, Eur. J. Inorg. Chem. 2017 (2017) 1549–1560.
[17] E. Alessio, Thirty years of the drug candidate NAMI-A and the myths in the field of ruthenium anticancer compounds: a personal perspective, Eur. J. Inorg. Chem. 2017 (2017) 1549–1560.
[18] E. Alessio, L. Messori, NAMI-A and KP1019/1339, two iconic ruthenium anticancer drug candidates face-to-face: a case story in medicinal inorganic chemistry, Molecules 24 (2019) 1995.

[19] R. Trondl, P. Heffeter, C.R. Kowol, M.A. Jakupec, W. Berger, B.K. Keppler, NKP-1339, the fi rst ruthenium-based anticancer drug on the edge to clinical application, Chem. Sci. 5 (2014) 2925–2932.
[20] B. Kumar Pragti, S. Mukhopadhyay Kundu, Target based chemotherapeutic advancement of ruthenium complexes, Coord. Chem. Rev. 448 (2021) 214169.
[21] A.A. Nazarov, C.G. Hartinger, P.J. Dyson, Opening the lid on piano-stool complexes: an account of ruthenium(II) e arene complexes with medicinal applications, J. Organomet. Chem. 751 (2014) 251–260.
[22] M. Rausch, P.J. Dyson, P. Nowak-Sliwinska, Recent considerations in the application of RAPTA-C for cancer treatment and perspectives for its combination with immunotherapies, Adv. Therap. 2 (2019) 1900042.
[23] A. Weiss, R.H. Berndsen, M. Dubois, C. Müller, R. Schibli, A.W. Griffioen, P. J. Dyson, P. Nowak-Sliwinska, In vivo anti-tumor activity of the organometallic ruthenium(II)-arene complex [Ru(η6-p-cymene)-Cl_2(pta)] (RAPTA-C) in human ovarian and colorectal carcinomas, Chem. Sci. 5 (2014) 4742–4748.
[24] L. Biancalana, G. Pampaloni, S. Zacchini, F. Marchetti, Synthesis, characterization and behavior in water/DMSO solution of Ru(II) arene complexes with bioactive carboxylates, J. Organomet. Chem. 869 (2018) 201–211.
[25] S. Parveen, M. Hanif, S. Movassaghi, M.P. Sullivan, M. Kubanik, M.A. Shaheen, T. Söhnel, S.M.F. Jamieson, C.G. Hartinger, Cationic Ru(η6-p-cymene) complexes of 3-hydroxy-4-pyr(id)ones– lipophilic triphenylphosphine as co-ligand is key to HighlyStable and cytotoxic anticancer agents, Eur. J. Inorg. Chem. 1721–1727 (2017).
[26] S. Keller, Y. Ching Ong, Y. Lin, K. Cariou, G. Gasser, A tutorial for the assessment of the stability of organometallic complexes in biological media, J. Organomet. Chem. 906 (2020) 121059.
[27] A. Alguacil, F. Scalambra, A. Romerosa, A. Bento-Oliveira, F. Marques, I. Maximiano, R.F.M. de Almeida, A.I. Tomaz, A. Valente, Evaluation of the antiproliferative properties of CpRu complexes containing N-methylated triazaphosphaadamantane derivatives, Bioinorg. Chem. Appl. (2023) (Article ID 6669394).
[28] C. Teixeira-Guedes, A.R. Brás, R.G. Teixeira, A. Valente, A. Preto, Ruthenium(II)–cyclopentadienyl-derived complexes as new emerging anti-colorectal cancer drugs, Pharmaceutics 14 (2022) 1293.
[29] J.M. Walker, A. McEwan, R. Pycko, M.L. Tassotto, C. Gottardo, J. Th'ng, R. Wang, G.J. Spivak, [Tris(pyrazolyl)methane]ruthenium complexes capable of inhibiting cancer cell growth, Eur. J. Inorg. Chem. (2009) 4629–4633.
[30] H.R. Bigmore, S.C. Lawrence, P. Mountford, C.S. Tredget, Coordination, organometallic and related chemistry of tris(pyrazolyl)methane ligands, Dalton Trans. 635–651 (2005).
[31] D.L. Reger, Tris(pyrazolyl)methane ligands: the neutral analogs of tris(pyrazolyl) borate ligands, Comments Inorg. Chem. 21 (1999) 1–28.
[32] J. Cervinka, A. Gobbo, L. Biancalana, L. Markova, V. Novohradsky, M. Guelfi, S. Zacchini, J. Kasparkova, V. Brabec, F. Marchetti, Ruthenium(II) tris-pyrazolylmethane complexes inhibit cancer cell growth by disrupting mitochondrial calcium homeostasis, J. Med. Chem. 65 (2022) 10567–10587.
[33] E. Bortolamiol, F. Visentin, T. Scattolin, Recent advances in bioconjugated transition metal complexes for cancer therapy, Appl. Sci. 13 (2023) 5561.
[34] P. Chellan, P.J. Sadler, Enhancing the activity of drugs by conjugation to organometallic fragments, Chem. A Eur. J. 26 (2020) 8676–8688.
[35] M. Yang, U. Bierbach, Metal-containing pharmacophores in molecularly targeted anticancer therapies and diagnostics, Eur. J. Inorg. Chem. 1561–1572 (2017).
[36] W.D.J. Tremlett, D.M. Goodman, T.R. Steel, S. Kumar, A. Wieczorek-Błauz, F. P. Walsh, M.P. Sullivan, M. Hanif, C.G. Hartinger, Design concepts of half-sandwich organoruthenium anticancer agents based on bidentate bioactive ligands, Coord. Chem. Rev. 445 (2021) 213950.
[37] T.R. Steel, F. Walsh, A. Wieczorek-Błauz, M. Hanif, C.G. Hartinger, Monodentately-coordinated bioactive moieties in multimodal half-sandwich organoruthenium anticancer agents, Coord. Chem. Rev. 439 (2021) 213890.
[38] C. Sumitha, M. Ganeshpandian, Half-sandwich ruthenium arene complexes bearing clinically approved drugs as ligands: the importance of metal−drug synergism in metallodrug design, Mol. Pharm. 20 (2023) 1453–1479.
[39] G. Bresciani, J. Vančo, T. Funaioli, S. Zacchini, T. Malina, G. Pampaloni, Z. Dvořák, Z. Trávníček, F. Marchetti, Anticancer potential of diruthenium complexes with bridging hydrocarbyl ligands from bioactive alkynols, Inorg. Chem. 62 (2023) 15875–15890.
[40] A. Gobbo, S.A.P. Pereira, L. Biancalana, S. Zacchini, M.L.M.F.S. Saraiva, P.J. Dyson, F. Marchetti, Anticancer ruthenium(II) tris(pyrazolyl)methane complexes with bioactive co-ligands, Dalton Trans. 51 (44) (2022) 17050.
[41] A. Begleiter, M. Mowat, L.G. Israels, J.B. Johnston, Chlorambucil in chronic lymphocytic leukemia: mechanism of action, Leuk. Lymphoma 23 (1996) 187–201.
[42] D. Catovsky, M. Else, S. Richards, Chlorambucil—still not bad: a reappraisal, Clin. Lymphoma Myeloma Leuk. 11 (2011) 53–56.
[43] P. Nowak-Sliwinska, A. Weiss, E. Păunescu, C.M. Clavel, A.W. Griffioen, P. J. Dyson, Anti-angiogenic properties of chlorambucil derivatives with fluorous and hydrocarbon appendages, Med. Chem. Commun. 7 (2016) 1596–1603.
[44] A.A. Nazarov, S.M. Meier, O. Zava, Y.N. Nosova, E.R. Milaeva, C.G. Hartinger, P. J. Dyson, Protein ruthenation and DNA alkylation: chlorambucil-functionalized RAPTA complexes and their anticancer activity, Dalton Trans. 44 (2015) 3614–3623.
[45] X. Qin, L. Fang, F. Chen, S. Gou, Conjugation of platinum(IV) complexes with chlorambucil to overcome cisplatin resistance via a "joint action" mode toward DNA, Eur. J. Med. Chem. 137 (2017) 167–175.
[46] S. Schoch, M. Hadiji, S.A.P. Pereira, M.L.M.F.S. Saraiva, S. Braccini, F. Chiellini, T. Biver, S. Zacchini, G. Pampaloni, P.J. Dyson, F. Marchetti, A strategy to conjugate bioactive fragments to cytotoxic diiron bis(cyclopentadienyl) complexes, Organometallics 40 (2021) 2516–2528.
[47] B. Neises, W. Steglich, Simple method for the esterification of carboxylic acids, Angew. Chem. Int. Ed. Engl. 17 (1978) 522–524.
[48] G. Bresciani, N. Busto, V. Ceccherini, M. Bortoluzzi, G. Pampaloni, B. Garcia, F. Marchetti, Screening the biological properties of transition metal carbamates reveals gold(I) and silver(I) complexes as potent cytotoxic and antimicrobial agents, J. Inorg. Biochem. 227 (2022) 111667.
[49] A. Levina, D.C. Crans, P.A. Lay, Speciation of metal drugs, supplements and toxins in media and bodily fluids controls in vitro activities, Coord. Chem. Rev. 352 (2017) 473–498.
[50] D.L. Reger, Syntheses of tris(pyrazolyl)methane ligands and {[tris(pyrazolyl) methane]Mn(CO)3}SO3CF3 complexes: comparison of ligand donor properties, J. Organomet. Chem. 607 (2000) 120–128.
[51] F. Menges, "Spectragryph - optical spectroscopy software", Version 1.2.5, @ 2016–2017. http://www.effemm2.de/spectragryph, 2024.
[52] G.R. Fulmer, A.J.M. Miller, N.H. Sherden, H.E. Gottlieb, A. Nudelman, B.M. Stoltz, J.E. Bercaw, K.I. Goldberg, NMR chemical shifts of trace impurities: common laboratory solvents, organics, and gases in deuterated solvents relevant to the organometallic chemist, Organometallics 29 (2010) 2176–2179.
[53] W. Willker, D. Leibfritz, R. Kerssebaum, W. Bermel, Gradient selection in inverse heteronuclear correlation spectroscopy, Magn. Reson. Chem. 31 (1993) 287–292.
[54] G.M. Sheldrick, SADABS-2008/1 - Bruker AXS Area Detector Scaling and Absorption Correction, Bruker AXS, Madison, Wisconsin, USA, 2008.
[55] G.M. Sheldrick, Crystal structure refinement with SHELXL, Acta Cryst. C 71 (2015) 3.
[56] N.M. Rice, H.M.N.H. Irving, M.A. Leonard, Nomenclature for liquid-liquid distribution (solvent extraction) (IUPAC Recommendations 1993), Pure Appl. Chem. 65 (1993) 2373–2396.
[57] a OECD Guidelines for Testing of Chemicals vol. 107, OECD, Paris, 1995; b J.C. Dearden, G.M. Bresnen, The measurement of partition coefficients, Quant. Struct.-Act. Relat. 7 (1988) 133–144.
[58] L. Biancalana, L.K. Batchelor, T. Funaioli, S. Zacchini, M. Bortoluzzi, G. Pampaloni, P.J. Dyson, F. Marchetti, α-diimines as versatile, derivatizable ligands in ruthenium (II) p-cymene anticancer complexes, Inorg. Chem. 57 (2018) 6669–6685.
[59] D.J. Currie, C.E. Lough, R.F. Silver, H.L. Holmes, Partition coefficients of some conjugated heteroenoid compounds and 1,4-naphthoquinones, Can. J. Chem. 44 (1966) 1035–1043.
[60] T. Rundlöf, M. Mathiasson, S. Bekiroglu, B. Hakkarainen, T. Bowden, T. Arvidsson, Survey and qualification of internal standards for quantification by 1H NMR spectroscopy, J. Pharm. Biomed. Anal. 52 (2010) 645–651.
[61] a C.C. Westcott, pH Measurements, Academic Press, New York, 1978; b A.K. Covington, M. Paabo, R.A. Robinson, R.G. Bates, Use of the glass electrode in deuterium oxide and the relation between the standardized pD (paD) scale and the operational pH in heavy water, Anal. Chem. 40 (1968) 700–706. Calculated by the formula pD = pH* + 0.4, where pH* is the value measured for H2O-calibrated pH-meter.